

# RSC Advances



This is an *Accepted Manuscript*, which has been through the Royal Society of Chemistry peer review process and has been accepted for publication.

*Accepted Manuscripts* are published online shortly after acceptance, before technical editing, formatting and proof reading. Using this free service, authors can make their results available to the community, in citable form, before we publish the edited article. This *Accepted Manuscript* will be replaced by the edited, formatted and paginated article as soon as this is available.

You can find more information about *Accepted Manuscripts* in the [Information for Authors](#).

Please note that technical editing may introduce minor changes to the text and/or graphics, which may alter content. The journal's standard [Terms & Conditions](#) and the [Ethical guidelines](#) still apply. In no event shall the Royal Society of Chemistry be held responsible for any errors or omissions in this *Accepted Manuscript* or any consequences arising from the use of any information it contains.

## Investigation of interfacial and photoelectrochemical characteristics of thermally treated PbS/TiO<sub>2</sub> photoanodes

Qiang Dong, Wei Liao, Bin Wang, Zhongqing Liu\*

*College of Chemical Engineering, Sichuan University, Chengdu 610065, Sichuan, PR China*

**Abstract:** Photoanodes composed of PbS QD sensitized TiO<sub>2</sub> nanotube arrays (PbS/TNAs) were prepared via the series ion layer adsorption replacement (SILAR) method. The samples were analyzed with X-ray diffraction (XRD), X-ray photoelectron spectroscopy (XPS), transmission electron microscope (TEM), UV-visible diffuse reflectance spectroscopy (UV-vis DRS), and photoluminescence (PL) to illustrate the sample microscopic morphologies, chemical composition, and light absorption properties. Current-potential ( $J-V$ ), current-time ( $I-t$ ), electrochemical impedance spectroscopy (EIS), and Mott-Schottky analyses revealed the charge transport and interfacial features in samples. The effects of thermal treatments on PbS/TNAs interfacial contacts and photoelectrochemical properties were systematically investigated. Under different atmospheres (air, vacuum, N<sub>2</sub>) during the thermal treatment, the crystal phase and chemical composition, light absorption, PbS quantum dot size and exposed crystal face, flat band potential, and resistance traits changed accordingly. When the sample was heated in N<sub>2</sub>, part of the PbS QDs was oxidized to form PbS@PbSO<sub>4</sub> junction. The size of the quantum dots increased from 4–5 nm to 14–15 nm, and the exposed crystal face changed from {111} to {200}. The interfacial resistances between PbS and TiO<sub>2</sub> increased as well. When the samples were thermally treated in air or vacuum, PbS QDs were mostly oxidized to PbSO<sub>4</sub>. After the electrodes were immersed in sulfur-containing electrolyte, PbSO<sub>4</sub> was vulcanized to PbS. Due to the limited mass transport across the newly formed PbS layer, the reduction was hardly complete. A PbSO<sub>4</sub>@PbS junction was formed with the new PbS having exposed crystal face of {220} instead of {111}. The sample not thermally treated boasted the best photoelectrochemical features with a short circuit current density of 7.04 mA.cm<sup>-2</sup>. The sample thermally treated in N<sub>2</sub> embraced the worst photoelectrochemical traits with a short circuit current density of 3.0 mA.cm<sup>-2</sup>.

**Keywords:** PbS quantum dots; TiO<sub>2</sub> nanotube arrays, SILAR; EIS; Mott-Schottky

## 1. Introduction

In 1972, Fujishima and Honda discovered that under photoirradiation, TiO<sub>2</sub> electrodes were able to electrolyze water to produce hydrogen.<sup>1</sup> Since the discovery, TiO<sub>2</sub> has attracted widespread interests in photovoltaic catalysis and solar cells because of its low-cost synthesis, low toxicity, and chemical stability. However, the wide bandgap of TiO<sub>2</sub> crystals (3.2 eV, anatase) precludes their accessibility to 45% of sunlight energy. And the very high recombination rates of the photoexcited electron-hole pairs further lower the power conversion efficiencies. For example, if the photoanode is made of anatase TiO<sub>2</sub> crystals, under the standard sunlight irradiation (AM 1.5G), the highest theoretical power conversion efficiency (PCE) is only 1.3%. The actual PCE of the solar cell presented in Fujishima's study was 0.1%. A primary research objective as well as an enormous challenge in this area is to expand the visible light response range of TiO<sub>2</sub> materials and to enhance the PCE by reducing the recombination rates of the photoexcited charge carriers.

In optoelectronic devices, the photoanode is the energy conversion element. The materials selection and structural design have become a major bottleneck of improving the device PCE. In recent years, there have been attempts of employing coupled narrow bandgap quantum dots (QDs) and highly ordered TiO<sub>2</sub> nanotubes to assemble photoanodes with adjustable absorbance edges.<sup>2-5</sup> Within these photoanodes, the heterojunction formed between QDs and TiO<sub>2</sub> also helps accelerated dissociation of the photoexcited charge carriers, and generates multiple-excitons by one absorbed photon. This method has become a highly effective means for enhanced optoelectronics performance of TiO<sub>2</sub>-based photoanodes. Among narrow bandgap semiconductors, lead chalcogenides are well known and widely investigated for their big Bohr exciton radii and narrow bandgaps.<sup>6,7</sup> For instance, PbS has a Bohr exciton radius of 18 nm and an intrinsic bandgap of 0.41 eV. Lead chalcogenides also boast high degenerated first excited states, mirror-imaged conduction bands and valence bands, energy levels matching that of TiO<sub>2</sub>, and long exciton lifetimes (200–800 s). Zhao et al utilized series ion deposition to infiltrate PbS QDs onto TiO<sub>2</sub> nanotube electrodes.<sup>8</sup> They obtained the optimized optoelectronic characteristics when the deposition times arrived 15. Grimes et al found that the optoelectronic properties of the PbS QD sensitized TiO<sub>2</sub> nanotube array photoanodes

relied on the modification procedure.<sup>9</sup> The photocurrent of the sample made from SILAR was  $11.02 \text{ mA}\cdot\text{cm}^{-2}$ , while that of the sample produced by electro-deposition was  $5.72 \text{ mA}\cdot\text{cm}^{-2}$ . Lian et al applied transient photo-absorption spectroscopy to study the dynamics of electron transfer from PbS QDs to  $\text{TiO}_2$  nanocrystals.<sup>10</sup> Their results demonstrate the possibility of extracting hot charge carriers and multiple-excitons. They also studied the dynamics of multiple-exciton generation and quenching by utilizing PbS QD/methylene blue complex as the QD/electron acceptor model. They illustrated that the generation and dissociation rates of multiple-excitons were not influenced by existence of QD charges and acceptors. Semonin et al reported the solar cells consisted of PbSe QDs that featured an external quantum efficiency of  $114\pm 1\%$  and internal quantum efficiency of  $130\%$ .<sup>11</sup> This is the first example that has an external quantum efficiency above 100% under low illumination intensities. The study also proves the likelihood of acquiring and fully utilizing multiple-excitons.

For semiconductor nanocrystals with diameters smaller than 10 nm, electrons are confined within the 3D potential wells. There is no free charge carrier generated upon illumination by light. Instead, bonded electron-hole excitons are generated. Excitons then diffuse to the internal interfaces of the photoelectrodes. Dissociation at the interfaces produces free charge carriers.<sup>12–15</sup> Interfaces between QD and  $\text{TiO}_2$  are formed when decorating  $\text{TiO}_2$  with QDs. The individual crystal face alignment, interfacial barrier, and QD size all contribute profoundly to the processes of exciton diffusion, transport, dissociation, and transfer.<sup>16–19</sup> In the directly coupled QD/ $\text{TiO}_2$  system made with SILAR, the ultrafast electron transfer from CdS to  $\text{TiO}_2$  occurs within 10–50 ps.<sup>20</sup> On the other hand, in the indirectly coupled QD/ $\text{TiO}_2$  system produced with self-assembled monolayer by using dual functional thiocarboxylic acid group, the impedance to electron transfer increases with longer molecular length.<sup>21</sup> In the ultrafast pump-probe laser spectroscopy technique study carried out by Grätzel et al, the dissociation rate at the PbS QD/(001)  $\text{TiO}_2$  interface is five times faster than that at the PbS QD/(101)  $\text{TiO}_2$  interface.<sup>22</sup> The transfer characteristics of the photoelectrons from PbS QDs to  $\text{TiO}_2$  can be controlled by adjusting the size of the QDs.<sup>23</sup> When using  $\text{TiO}_2$  nanobelts to replace  $\text{TiO}_2$  nanoparticles, the nanohybrids of PbS-QD/ $\text{TiO}_2$ -NB absorbs light up to 1400 nm. Study of the interfacial transfer properties and limiting factors of the narrow bandgap semiconductor QDs (such as PbS) and wide bandgap semiconductors (such as  $\text{TiO}_2$ ) pertains

great scientific significance for the improvement of optoelectronic performance of such systems.

In the current study, we use the SILAR method to prepare PbS sensitized TiO<sub>2</sub> nanotube arrays electrode (PbS/TNAs) by employing dual functional thioacetic acid as a linkage.<sup>24–26</sup> Since PbS is a relatively unstable material, it can be oxidized to PbSO<sub>4</sub> as the final product.<sup>47</sup> Therefore, we systematically investigated the effects of thermal treatment under different level of oxidation conditions (air > vacuum > N<sub>2</sub>) and temperature on the interfacial contact and optoelectronic properties. The relationship between the structure and properties was analyzed by X-ray diffraction (XRD), X-ray photoelectron spectroscopy (XPS), transmission electron microscope (TEM), UV-visible diffuse reflectance spectroscopy (UV-vis DRS), photoluminescence (PL), electrochemical impedance, and Mott-Schottky. Our results indicate that the thermal treatment induces surface oxidation, enlargement of the PbS QD size, and alternation of the exposed crystal faces. The changes lead to diminished interfacial contact between PbS and TiO<sub>2</sub> and apparently increased impedance. The interfacial charge transfer becomes hindered and the overall optoelectronic performance is decreased.

## 2. Experimental

### 2.1 Sample preparation

The detailed procedure and conditions of electrochemical anodization preparation of TiO<sub>2</sub> nanotube arrays (TNAs) are reported in our previous work.<sup>27–29</sup> The high purity titanium sheet was mechanical polished before chemical polishing. Then anodic oxidation was operated using polished Ti sheet as anode, high purity graphite sheet as the counter electrode at 60V for 4h. The electrolyte was an ethylene glycol solution with 0.2wt.% HF, 0.5wt.% NH<sub>4</sub>F, 2vol.% H<sub>2</sub>O. After the anodic oxidation, the TNAs were washed with deionized water and ethanol repeatedly, after which they were annealed at 500 °C for 2h to obtain anatase TNAs. After removing the plugging matters on the TNA openings by ultrasonication in 10 vol.% H<sub>2</sub>O<sub>2</sub>, the TNAs were heated at 500 °C in air for 2 h to convert amorphous TiO<sub>2</sub> to anatase TiO<sub>2</sub>. To replenish the removed hydroxyl groups during the thermal treatment, the thermally crystallized TNAs were immersed in 5 g L<sup>-1</sup> NaOH for 4 h. After rinse with water, the TNAs were immersed in 0.02 M thioacetic acid (TGA) for 4 h. The TNAs were again rinsed with

water and dried by air. Using 0.002 M  $\text{Pb}(\text{NO}_3)_2$  and 0.005 M  $\text{Na}_2\text{S}$  as the Pb and S sources, respectively, series ion layer adsorption replacement (SILAR) was performed on the materials. One SILAR cycle containing  $\text{Pb}(\text{NO}_3)_2$ -rinse and drying- $\text{Na}_2\text{S}$ -rinse and drying took 60 s. The PbS sensitized TNAs (PbS/TNAs) were prepared with ten SILAR cycles. Different samples were further heated at  $10\text{ }^\circ\text{C min}^{-1}$  and kept at  $300\text{ }^\circ\text{C}$  for 2 h in air, vacuum, and  $\text{N}_2$ , respectively. The corresponding samples were labeled A-PbS/TNAs, V-PbS/TNAs, and N-PbS/TNAs, while the thermally untreated sample was labeled U-PbS/TNAs.

## 2.2 Characterization

XRD (Philips XPert pro MPD) analysis provided the crystalline phase information of the samples. TEM (Tecnai G2 F20 S-Twin) demonstrated the microscopic morphologies. XPS (Kratos XSAM-800) presented the chemical composition. PL (F-7000) afforded the dissociation properties of photoinduced charge carriers with an excitation wavelength of 300 nm.

## 2.3 Photoelectrochemical analysis

The photoelectrochemical analyses were performed on CHI650E electrochemical workstation (Chenhua, Shanghai), including  $J-V$ ,  $I-t$ , photocurrent attenuation, EIS, and Mott-Schottky analysis. The light source was AM1.5G ( $100\text{ mW cm}^{-2}$ ). The sample was used as the working electrode, a Pt tile as the counter electrode, SCE as the reference electrode, and  $0.1\text{ M Na}_2\text{S} + 0.1\text{ M Na}_2\text{SO}_3$  as the supporting electrolyte.

# 3. Results and discussion

## 3.1 Sample characterization

Figure 1 shows the XRD patterns of the samples. According to Figure 1a, the pristine TNAs only contains diffractions of Ti baseline and anatase  $\text{TiO}_2$ . After the deposition of PbS, the thermally untreated U-PbS/TNAs (Fig. 1b) demonstrates broadened  $\{111\}$ ,  $\{200\}$ , and  $\{220\}$  diffraction peaks of PbS as well as Ti baseline and anatase  $\text{TiO}_2$  (JCPDS#05-0592).<sup>8,9</sup> Sample N-PbS/TNAs, thermally treated under  $\text{N}_2$ , possesses the same diffractions as U-PbS/TNAs. For samples A-PbS/TNAs and V-PbS/TNAs, the PbS diffraction patterns at  $\{111\}$ ,  $\{200\}$ , and  $\{220\}$  disappeared. Instead, diffractions at  $\{101\}$ ,  $\{111\}$ , and  $\{210\}$  of  $\text{PbSO}_4$  (JCPDS#36-1461) illustrate the oxidation of PbS QDs.<sup>31,32</sup> Figure S<sub>2</sub> was generated by

fractioning the spectra because of the partial overlapping of PbS {111} diffraction and anatase TiO<sub>2</sub> {101} diffraction. In Figure S<sub>2</sub>, the PbS {111} diffraction of sample N-PbS/TNAs is obviously weaker than that of sample U-PbS/TNAs, yet the intensities of diffraction peaks at {200}, {220} are almost identical. This is probably due to the result of reorientation of crystal face alignment after thermal treatment.

XPS was performed on the 300 °C treated samples A-PbS/TNAs, V-PbS/TNAs, and N-PbS/TNAs to shed light on the surface chemical composition changes induced by different heat-treatment atmospheres (Figure 2). From the Figure, it is demonstrated that all samples contain Ti, O, Pb, and S. From the high resolution XPS, the elemental composition percentage of each element can be quantified and the results are tabulated in Table S<sub>1</sub>. In all samples, the Pb/S atomic ratio is greater than 1, while the value decreases according to treatment atmosphere of air, vacuum, and N<sub>2</sub>. We attribute the phenomenon to the oxidation of S<sup>2-</sup> of the PbS QDs into volatile S<sup>0</sup> or SO<sub>2</sub>. Under air, the atmosphere is the most oxidizing, so the highest amount of oxidized S that leads to the greatest Pb/S ratio of 1.76. Under N<sub>2</sub> the atmosphere is the least oxidizing, so the lowest amount of oxidized S leading to the lowest Pb/S ratio of 1.55, while the ratio is 1.61 under vacuum due to the oxidizing atmosphere is between the N<sub>2</sub> and air. The oxygen source under vacuum or N<sub>2</sub> atmosphere could be from hydroxyl groups adsorbed on PbS/TNAs before heat treatment during the aqueous SILAR manipulations.

The Pb<sub>4f</sub> and S<sub>2s</sub> XPS high resolution binding energy profiles of A-PbS/TNAs, V-PbS/TNAs, and N-PbS/TNAs are shown in Figures 3 and 4, respectively, to illustrate Pb and S oxidation states. After thermal treatment at 300 °C for 2 h under air and vacuum, the binding energies of Pb<sub>4f</sub> appear at 143.2 eV and 138.4 eV, matching that of Pb in PbSO<sub>4</sub>. Besides the two binding energies of Pb in PbSO<sub>4</sub>, there are two Pb peaks at 141.8 eV and 137.1 eV after thermal treatment at 300 °C for 2 h under N<sub>2</sub>, matching that of Pb<sup>0</sup>. In Figure 4, the binding energy of S<sub>2s</sub> appears at 232.3 eV after thermal treatment at 300 °C for 2 h under air and vacuum, corresponding to that of S in PbSO<sub>4</sub>.<sup>32,33</sup> Besides the binding energy of S in PbSO<sub>4</sub>, there is one S peak at 224.6 eV after thermal treatment at 300 °C for 2 h under N<sub>2</sub>, matching that of S in PbS. The atomic ratio of this S oxidation state is 87.12%.

Figure 5 exhibits the transmission electron microscope images of U-PbS/TNAs and

N-PbS/TNAs. In Fig. 5a and 5c, uniformly formed PbS nanoparticles are visible. The size distribution of the nanoparticles is illustrated in Figure 6. The average particle size in U-PbS/TNAs is 4–5 nm (Fig. 6a). After thermal treatment at 300 °C for 2 h under N<sub>2</sub>, the average size grows to 14–15 nm (Fig. 6b). The high resolution TEM images of Fig. 5b and 5d further reveal the fine crystal structures of PbS QDs. In Fig. 5b, the interplanar distance of 0.342 nm corresponds to PbS {111} crystal face. The interplanar spacing value of 0.297 nm is from PbS {200} crystal face (Fig. 5d).<sup>8,34</sup>

When the samples were thermally treated in air or vacuum, PbS QDs were mostly oxidized to PbSO<sub>4</sub>, besides the colour of the samples changed from black (PbS) to its original TiO<sub>2</sub> colour. After the electrodes were immersed in sulfur-containing electrolyte, the colour of the samples changed to black again. Thus, it can be convinced that PbSO<sub>4</sub> was vulcanized to PbS. The TEM and HRTEM images of sample A-PbS/TNAs after immersed in the 0.1 M Na<sub>2</sub>S + 0.1 M Na<sub>2</sub>SO<sub>3</sub> are shown in Figure S<sub>2</sub>. The SO<sub>4</sub><sup>2-</sup> of PbSO<sub>4</sub> formed during the thermal treatment of the PbS/TNAs may have undergone ion exchange with S<sup>2-</sup> in solution to generate PbS nanoparticles by vulcanization. The density of the newly formed PbS nanoparticles is smaller than that of the thermally untreated U-PbS/TNAs, while the exposed PbS nanoparticle crystal face is {220}.<sup>35,36</sup> Considering the hindrance of the newly formed PbS layer against the outward diffusion of SO<sub>4</sub><sup>2-</sup> as well as the inward diffusion of S<sup>2-</sup>, it is probable that PbSO<sub>4</sub> can hardly become completely vulcanized. The combined results of XRD, XPS, and TEM analyses demonstrate the formation of PbSO<sub>4</sub>@PbS{220} junction when the samples thermally treated in air or vacuum are placed in the electrolyte. For the samples thermally treated in N<sub>2</sub>, PbS{200}@PbSO<sub>4</sub>@PbS{220} junction is formed in the process. The surface oxidation of the PbS/TNAs samples after thermal treatment, combined with the enlargement of PbS nanoparticles and variation in exposed crystal faces, will change the microscopic unit interfaces of the photoelectrodes and impact the interfacial charge dissociation and transfer.

Figure 7 displays the UV-vis diffuse absorbance spectra of the samples. The thermally untreated sample shows strong absorption in the visible range. For the samples after thermal treatment at 300 °C for 2 h under air and vacuum, their absorption curves are weaker than that of U-PbS/TNAs and close to that of TNAs. The oxidation induced by heat treatment generates PbSO<sub>4</sub> or PbS@PbSO<sub>4</sub> junctions that efficiently blocks light absorption and transmission

hence the low absorption.

According to Kubelka–Munk equation:<sup>37,38</sup>

$$ah\nu = A(h\nu - E_g)^n \quad (1)$$

here,  $a$  is the absorption coefficient,  $h\nu$  is the photon energy,  $E_g$  is the bandgap width.  $\text{TiO}_2$  is a direct transition semiconductor so  $n$  takes 1/2. When plotting  $h\nu$  against  $ah\nu$ , the intercept by the extension of the tangent line of the linear portion curve and the horizontal axis represents the semiconductor bandgap. The TNAs without PbS sensitization has a bandgap of 3.11 eV. After thermal treatment at 300 °C for 2 h under air and vacuum, the samples A-PbS/TNAs and V-PbS/TNAs have bandgap energies at 2.91 eV and 2.99 eV, respectively. Sample U-PbS/TNAs has a bandgap of 2.34 eV, indicating its absorption cut off value of 529 nm.

### 3.2 Photoelectrochemical analysis

The J–V curves of the samples are shown in Figure 8. The pristine sample has a short circuit photocurrent density of 0.44  $\text{mA}\cdot\text{cm}^{-2}$ , while that of the sensitized, thermally untreated PbS/TNAs is 7.04  $\text{mA}\cdot\text{cm}^{-2}$ , an increase of 16 times in magnitude. This demonstrates the potential of improving power conversion efficiency by PbS QD sensitization of  $\text{TiO}_2$ . After thermal treatment at 300 °C for 2 h under air, vacuum or  $\text{N}_2$ , the photocurrent densities of the samples decrease to  $\sim 3 \text{ mA}\cdot\text{cm}^{-2}$ . Figure S<sub>3</sub> shows the J–V curves of PbS/TNAs samples after thermal treatment at various temperatures under air. It is obvious that with increasing treatment temperature, the short circuit photocurrent density decreases. The reason might be that at higher temperatures, the oxidation degrees of the PbS QDs in PbS/TNAs are high. There is evidence of vulcanization when the arrays are immersed in electrolyte. Albeit, the newly formed PbS layer hinders the transfer process during vulcanization leading to the formation of  $\text{PbSO}_4$ @PbS junction. The insulating  $\text{PbSO}_4$  layer between PbS and  $\text{TiO}_2$  becomes a recombination center for photoinduced charge carriers. This is shown in the photoluminescence curves in Figure S<sub>4</sub>. All samples have the similar PL shape and wavelength, indicating they possess the same bandgap structures. The thermally untreated PbS/TNAs sample has the weakest emission intensity, illustrating the lowest possibility of recombination of photoinduced charge carriers after photoirradiation. The PL emission intensities of the V-PbS/TNAs and N-PbS/TNAs are slightest weaker than that of the pristine

TNAs, but much stronger than that of U-PbS/TNAs. The samples with stronger PL intensities present high possibilities of recombination of photoinduced charge carriers. The schematics of carriers transmission on the interface of the samples are shown in Fig S<sub>8</sub>. The distance between two dotted lines represent the ability of transmittability

According to XRD, XPS, TEM, and UV-vis DRS results, thermal treatment causes oxidation on PbS of the PbS/TNAs samples that leads to less absorption in the visible range. PbS QDs also grow in size and the exposed crystal face changes from {111} to {200}. Less absorption brings lower light utilization efficiency. The enlarged PbS nanoparticles reduces the total contact area between PbS and TiO<sub>2</sub>. The reduced quantum size effect can decrease the chemical energy gradient between the two semiconductors. The mismatch degree of the different interface contact types is calculated by the following equation.

$$\delta = \frac{2|a_1 - a_2|}{a_1 + a_2}$$

$\delta$  is the mismatch degree,  $a_1$  and  $a_2$  are the lattice distance of the certain faces for the two semiconductors.

When PbS QDs have {111} as the exposed crystal face, the mismatch with TiO<sub>2</sub> {101} lattice is 2.88%. When the exposed crystal face of PbS is {200}, the mismatch with TiO<sub>2</sub> {101} becomes 16.95%. It is convinced that when the mismatch is less than 5%, the interface is coherent interface. While when the mismatch is greater than 5% and less than 25%, the interface is half coherent interface. The lattice mismatch increases significantly after PbS exposed crystal face changes from {111} to {200}. This change in turn aggravates the interfacial recombination, as well as impairs the interfacial contact. The electron wave function overlap of the contact is diminished. These alterations bring reduced dissociation, transport, and transfer rates, but intensified recombination of the photoinduced excitons at the PbS and TiO<sub>2</sub> interfaces. These detrimental factors brought about by the thermal treatment of PbS/TNAs samples result in lower photon to electron conversion efficiency.

We performed photocurrent attenuation tests on the samples to better understand the transport properties of the photoinduced charge carriers. Figure 9 shows the photocurrent attenuation curves of the samples recorded every 10  $\mu$ s. The initial inflection point of the photocurrent density decrease is the point-in-time when photoirradiation is turned off. Using

the initial inflection point as the starting time when the photocurrent is stabilized, the photocurrent attenuation rate in the circuit of the samples are recorded after photoirradiation is turned off. From Fig. 9, the pristine TNAs has the lowest photocurrent attenuation rate at  $0.225 \text{ mA}\cdot\text{cm}^{-2}\cdot\text{s}^{-1}$ . And the U-PbS/TNAs has the highest photocurrent attenuation rate at  $16.655 \text{ mA}\cdot\text{cm}^{-2}\cdot\text{s}^{-1}$ , 74 times in magnitude of that of pristine TNAs. The photocurrent attenuation rate reflexes the transport efficiency of photoinduced charge carriers. Higher rates are related to faster transport efficiencies, i.e., the rates that charge carriers are transported to and consumed in the exterior circuit.<sup>19,39,40</sup> The U-PbS/TNAs has the highest photocurrent attenuation rate manifesting that its interfaces enjoy the most efficient dissociation, transport, and transfer rates. This type registers the greatest photocurrent density among samples analyzed. The photocurrent attenuation results match the  $J-V$  analysis results.

Electrochemical alternating impedance experiments can characterize the kinetics of electrode process and electrode surface process by measuring the responses of a system toward the external small sinusoidal disturbances. For pure resistance circuits, the Nyquist plot should display the simple linear unit characteristics, a point within the positive quadrant. For a system with a capacitor, the Nyquist plot resembles an arc whose size quantifies the capacitance.<sup>41-43</sup> Figure 10 shows the Nyquist plots of samples undergoing different treatments. Compared to the pristine TNAs, the samples sensitized with PbS QDs show diminished impedances, representing optimized dissociation and transport of the photoinduced charge carriers. For samples undergoing different thermal treatments, they all display similar the impedance type. The A-PbS/TNAs has the smallest impedance while the N-PbS/TNAs has the greatest impedance.

The electrochemical system can be represented with an equivalent circuit according to the shape of the electrochemical impedance spectroscopy (EIS).<sup>44,45</sup> Figure S<sub>5</sub> displays the alternating impedance and simulated equivalent circuit of the pristine TNAs. Figure S<sub>6</sub> is a similar representation of N-PbS/TNAs, while Figure S<sub>7</sub> is that of U-PbS/TNAs. Table 1 displays the simulated values of the devices in equivalent circuits. According to the simulated equivalent circuit, there exists a metal-semiconductor contact interface between Ti and TiO<sub>2</sub> as well as a contact interface between TiO<sub>2</sub> and the electrolyte in pristine TNAs. For the PbS/TNAs, there is one more PbS/TiO<sub>2</sub> contact interface besides the abovementioned two

interfaces. Each of the interfaces is treated as a series resistance-capacitance unit. From Table 1, the resistance  $R_1$  representing the Ti/TiO<sub>2</sub> interface is reduced after thermal treatment at 300 °C. Twice-annealing helps the interfacial contact between Ti/TiO<sub>2</sub>. The increased values of  $R_2$  and  $C_2$  suggest the enlarged resistance between PbS and TiO<sub>2</sub>. After thermal treatment, the PbS QDs grow in size, and the interfacial contact changes from PbS{111}/TiO<sub>2</sub>{101} to PbS{200}/TiO<sub>2</sub>{101}. The change is characterized by the shrunk contact area and lowered interfacial chemical energy gradient, plus diminished interfacial electronic wave function overlap. The changes in  $R_3$  and  $C_3$  disclose the reduced resistances between TiO<sub>2</sub> and electrolyte after sensitized by PbS QDs. The thermal treatment increases such resistances, the result of the resistance between PbS{111} and electrolyte being less than that between PbS{200} and electrolyte. The Warburg resistance  $R_W$  of the electrode process denotes the concentration polarization effect of the electrode process. Its value refers to the charge carrier consumption by the diffusion at the electrode surface. A high  $R_W$  indicates strengthened transport efficiency of the internal electrode charge carriers, and the electrode surface reaction is controlled by the diffusion process. By analyzing the equivalent circuit, charge transport in the pristine TNAs is controlled by the interfacial resistance between Ti and TiO<sub>2</sub> ( $R_1 = 85.33$ ). The thermally treated electrodes are dominated by the interfacial resistance between PbS and TiO<sub>2</sub> ( $R_2 = 165.8$ ). The overall resistance of the PbS/TNAs electrode after thermal treatment is  $209.62 \Omega \text{ cm}^2$ , greater than  $118.88 \Omega \text{ cm}^2$  of the pristine PbS/TNAs. The result is in accord with the photocurrent density analysis.

Mott-Schottky plot provides accurate information of the PbS/TNAs such as donor concentration  $N_d$  or acceptor concentration  $N_a$  and the flat band potential  $E_{fb}$ . Figure 11 shows the Mott-Schottky curves of different samples. In the linear parts of the curves, the slopes of the tangent lines are all positive, representing n-type semiconductors. The relationship between donor concentration  $N_d$  and flat band potential  $E_{fb}$  of n-type semiconductors can be expressed by the following equation:

$$\left(\frac{C}{A}\right)^{-2} = \frac{2}{eN_d\epsilon\epsilon_0} \left(E - E_{fb} - \frac{kT}{e}\right) \quad (2)$$

Here,  $N_d$  is the donor concentration,  $e$  is the electron charge of  $1.6 \times 10^{-19} \text{ C}$ ,  $\epsilon$  is the relative dielectric constant of 18,  $\epsilon_0$  is the dielectric constant of vacuum,  $E$  is the applied bias potential,

$k$  is the Boltzmann constant,  $T$  is the temperature, and  $A$  is the electrode area. The extension of the Mott-Schottky curve to  $1/C^2 = 0$  results in the flat band potential  $E_{fb}$ , and its slope denotes the  $N_d$ .

The flat band potentials of the samples relative to SCE are tabulated in Table S<sub>2</sub>. Under flat band conditions, the flat band potential of a semiconductor is equal to the Fermi energy. The lower the Fermi energy, the lesser the chemical potential gradient from the electrolyte to the semiconductor, the smaller the curvature of the semiconductor energy band, which in turns implies the slower charge carrier dissociation and transfer at the interface between the semiconductor and the electrolyte. The trend reverses with higher Fermi energy, leading to the faster charge carrier dissociation and transfer at the interface between the semiconductor and the electrolyte. According to Table S<sub>2</sub>, the pristine TNAs holds the most negative Fermi energy while U-PbS/TNAs has the most positive value. Therefore, at the interface between the semiconductor and electrolyte, the pristine TNAs has the smallest energy band curvature and U-PbS/TNAs the largest. Accordingly, U-PbS/TNAs embraces much faster charge carrier dissociation and transfer at that semiconductor and electrolyte interface than the pristine TNAs. For the thermally treated samples, the flat band potentials follow a positive to negative order of air > vacuum > N<sub>2</sub>. The most negative flat band potential of N-PbS/TNAS probably is caused by the donor doping of Pb<sup>0</sup>. The photoinduced charge carrier dissociation and transfer rates at the interface of semiconductor and electrolyte follows the order air > vacuum > N<sub>2</sub>, the same order of the photocurrent of the samples.

#### 4. Conclusion

Photoanodes of PbS QD sensitized TiO<sub>2</sub> nanotube arrays were prepared by the SILAR procedure. The effects of thermal treatment on microscopic morphologies, surface chemical composition, interfacial contact, and the photoelectrochemical characteristics of the PbS/TiO<sub>2</sub> photoanodes are systematically investigated. Our results unveil that thermal treatment leads to oxidation and enlargement of PbS QDs on the electrodes. The related changes of the exposed crystal face, light absorption property, interfacial resistance, and flat band potential contribute to the deteriorated photoelectrochemical performance. The U-PbS/TNAs absorption red shifts to 529 nm. Its interfacial resistance between PbS and TiO<sub>2</sub> is smaller than that of

N-PbS/TNAs while its flat band potential is more positive. These characteristics symbolize strong light absorption, fast interfacial charge carrier dissociation and transfer, thus high-quality photoelectrochemical performance. When the PbS/TiO<sub>2</sub> was thermally treated under air or vacuum, part of PbS was oxidized to volatile S<sup>0</sup> or SO<sub>2</sub> and PbSO<sub>4</sub>. The sulfate could be reduced by the electrolyte composed of Na<sub>2</sub>S and Na<sub>2</sub>SO<sub>3</sub>. But the newly formed PbS layer presented mass transport limit to produce the PbSO<sub>4</sub>@PbS{220} junction. The N-PbS/TNAs electrode encompassed PbS{200}@PbSO<sub>4</sub> junction and enlarged PbS nanoparticles, exposed crystal face changing from {111} to {200}. When the electrode was immersed in the electrolyte, the surface PbSO<sub>4</sub> on PbS was vulcanized to form PbS{200}@PbSO<sub>4</sub>@PbS{220} junction. The interfacial resistance between PbS and TiO<sub>2</sub> was increased and flat band potential shifted to negative. The results were weakened interfacial contact, lower photoinduced charge carrier dissociation and transfer rates, and poor photoelectrochemical performance.

### Acknowledgements

This work was supported by the National Science Foundation of China (Grant No. 50774053 and 21376154). The authors would like to express their heartfelt gratitude to Analytical and Test Center of Sichuan University.

### Notes and references

- 1 A. Fujishima, K. Honda, *Nature*, 1972, **238**, 37–38.
- 2 J. B. Sambur, T. Novet and B. A. Parkinson, *Science*, 2010, **330**, 63–66.
- 3 D. R. Baker, P. V. Kamat, *Adv. Funct. Mater.*, 2009, **19**, 805–811.
- 4 O. E. Semonin, J. M. Luther, S. Choi, H. Y. Chen, J. Gao, A. J. Nozik, M. C. Beard, *Science*, 2011, **334**, 1530–1533.
- 5 F. A. Frame, F. E. Osterloh, *J. Phys. Chem. C*, 2010, **114**, 10628–10633.
- 6 J. J. Peterson and T. D. Krauss, *Nano Lett.*, 2006, **6**, 510–514.
- 7 J. B. Sambur, T. Novet, B. A. Parkinson, *Science* 2010, **330**, 63–66
- 8 F. G. Cai, F. Yang, Y. Zhang, C. Ke, C. H. Cheng, Y. Zhao, G. Yan, *Phys. Chem. Chem. Phys.*, 2014, **16**, 23967–23974.
- 9 Q. Kang, S. H. Liu, L. X. Yang, Q. Y. Cai, C. A. Grimes, *ACS Appl. Mater. Interfaces*, 2011, **3**, 746–749.

- 10 Y. Yang, W. R. Córdoba, T. Q. Lian, *Nano Lett.*, 2012, **12**, 4235–4241.
- 11 O. E. Semonin, J. M. Luther, S. Choi, H. Y. Chen, J. B. Gao, A. J. Nozik, M. C. Beard, *Science*, 2011, **334**, 1530–1533.
- 12 R. Schaller, V. I. Klimov, *Phys. Rev. Lett.*, 2004, **92**, 186601–186604.
- 13 J. Huang, Z. Q. Huang, Y. Yang, H. M. Zhu, T. Q. Lian, *J. Am. Chem. Soc.*, 2010, **132**, 4858–4864.
- 14 H. M. Zhu, T. Q. Lian, *J. Am. Chem. Soc.*, 2012, **134**, 11289–11297.
- 15 A. J. Nozik, M. C. Beard, J. M. Luther, M. Law, R. J. Ellingson, J. C. Johnson, *Chem. Rev.*, 2010, **110**, 6873–6890.
- 16 L. X. Sang, H. Y. Tan, X. M. Zhang, Y. T. Wu, C. F. Ma, C. Burda, *J. Phys. Chem. C*, 2012, **116**, 18633–18640.
- 17 J. B. Gao, C. L. Perkins, J. M. Luther, M. C. Hanna, H. Y. Chen, O. E. Semonin, A. J. Nozik, R. J. Ellingson, M. C. Beard, *Nano Lett.*, 2011, **11**, 3263–3266.
- 18 P. Sudhagar, V. González-Pedro, I. Mora-Seró, F. Fabregat-Santiago, J. Bisquert, Y. S. Kang, *J. Mater. Chem.*, 2012, **22**, 14228–14235.
- 19 H. H. Yang, W. G. Fan, A. Vaneski, A. S. Susha, W. Y. Teoh, A. L. Rogach, *Adv. Funct. Mater.*, 2012, **22**, 2821–2829.
- 20 J. L. Blackburn, D. C. Selmarten, A. J. Nozik, *J. Phys. Chem. B*, 2003, **107**, 14154–14157.
- 21 D. Lawless, S. Kapoor, D. Meisel, *J. Phys. Chem.*, 1995, **99**, 10329–10335.
- 22 E. Ghadiri, B. Liu, J. E. Moser, M. Grätzel, L. Etgar, *Part. Part. Syst. Charact.*, 2014, DOI: 10.1002/ppsc.201400210
- 23 D. F. Wang, H. G. Zhao, N. Q. Wu, M. A. E. Khakani, D. L. Ma, *J. Phys. Chem. Lett.*, 2010, **1**, 1030–1035.
- 24 C. Ratanatawanate, C. Xiong, K. J. B. Jr, *ACS NANO*, 2012, **2**, 1682–1688.
- 25 R. Vogel, P. Hoyer, H. Weller, *J. Phys. Chem.*, 1994, **98**, 3183–3188.
- 26 W. T. Sun, Y. Yu, H. Y. Pan, X. F. Gao, Q. Chen, L. M. Peng, *J. Am. Chem. Soc.*, 2008, **130**, 1124–1125.
- 27 X. Liu, Z. Q. Liu, S. X. Hao, W. Chu, *Mater. Lett.*, 2012, **80**, 66–68.
- 28 G. Q. Ji, Z. Q. Liu, D. B. Guan, Y. T. Yang, *Appl. Surf. Sci.*, 2013, **282**, 695–699.
- 29 X. Liu, Z. Q. Liu, J. L. Lu, X. L. Wu, B. Xu, W. Chu, *J. Colloid Interf. Sci.*, 2014, **413**, 1723.
- 30 C. Arrouvel, M. Digne, M. Breyse, H. Toulhoat, P. Raybaud, *J. Catal.*, 2004, **222**, 152–156.
- 31 S. B. Bubenhofer, C. M. Schumacher, F. M. Koehler, N. A. Luechinger, R. N. Grass, W. J. Stark, *J. Phys. Chem. C*, 2012, **116**, 16264–16270.

- 32 S. D. Sung, I.Lim, P.I Kang, C. Lee, W.I.Lee, *Chem. Commun.*, 2013, **49**, 6054–6056.
- 33 E. J. D. Klem, D. D. MacNeil, L. Levina, E. H. Sargent, *Adv. Mater.*, 2008, **20**, 3433–3439.
- 34 H. Tada, M. Fujishima, H. Kobayashi, *Chem. Soc. Rev.*, 2011, **40**, 4232–4243.
- 35 Y.M.Zhu, R.L. Wang, W.P.Zhang, H.Y.Ge, L. Li, *Appl.Surf.Sci.*, 2014, **315**, 149–153.
- 36 B.H. Lee, H. C. Leventis, S.-Jin Moon, P. Chen, S. Ito, S.A. Haque, T.Torres, F. Nüesch, T.Geiger, S. M. Zakeeruddin, M. Grätzel, M. K. Nazeeruddin, *Adv. Funct. Mater.*, 2009, **19**, 2735–2742.
- 37 F. Dong, W. Zhao, Z. Wu, *Nanotechnology*, 2008, **19**, 365607–365616.
- 38 X.B. Chen, C. Burda, *J. Phys. Chem. B*, 2004, **108**, 15446–15449.
- 39 J. H. Bang, P. V. Kamat, *Adv. Funct. Mater.*, 2010, **20**, 1970–1976.
- 40 V. Chakrapani, D. Baker, P. V. Kamat, *J. Am. Chem. Soc.*, 2011, **133**, 9607–9615.
- 41 Z.Y.Liu, B.Pesic, K.S.Raja, R.R.Rangaraju, M.Misra, *Int.J. Hydrogen Energy*, 2009, **34**:3250–3257.
- 42 J.Bisquert, G. Garcia-Belmonte, F.Fabregat-Santiago, *J.Phys.Chem.B.*, 2000, **104**, 2287–2298.
- 43 J.Bisquert, *J.Phys.Chem.B.*, 2002, **106**, 325–333.
- 44 X.S.Li, Z.Y.Zhang, G.M.Bai, C.X.Du, C.F.Ma, *Int.J. Hydrogen Energy*, 2012, **37**, 854–859.
- 45 W. P.Gomes, D. Vanmaekelbergh, *Electrochim. Acta*, 1996, **41**, 967–973
- 46 S.E.John, S.K.Mohapatra, M.Misra, *Langmuir*, 2009, **25**, 8240–8247.
- 47 L.V.Yashina, A.S.Zyubin, R.Püttner, T.S.Zyubina, V.S.Neudachina, P.Stojanov, J.Riley, S.N.Dedyulin, M.M.Brzhezinskaya, V.I.Shtanov, *Surface Science*, 2011, **605(5)**, 473–482.

## Figure captions

**Fig.1.** XRD patterns of (a) pristine TNAs,(b) U-PbS/TNAs, (c) A-PbS/TNAs, (d) V-PbS/TNAs and (e) N-PbS/TNAs.

**Fig.2.** XPS profiles of (a) A-PbS/TNAs, (b) V-PbS/TNAs and (c) N-PbS/TNAs.

**Fig.3.** XPS profiles of  $Pb_{4f}$  of (a) A-PbS/TNAs, (b) V-PbS/TNAs and (c) N-PbS/TNAs

**Fig.4.** XPS profiles of  $S_{2s}$  of (a) A-PbS/TNAs, (b) V-PbS/TNAs and (c) N-PbS/TNAs

**Fig.5.** TEM and HRTEM images of the U-PbS/TNAs and N-PbS/TNAs.

**Fig.6.** Size distribution histograms of PbS nanoparticles for (a) U-PbS/TNAs and (b) N-PbS/TNAs.

**Fig.7.** UV-vis diffuse absorbance spectra of (a) pristine TNAs, (b) A-PbS/TNAs,(c)V- PbS/TNAs and (d) U-PbS/TNAs. The inset is the plots of  $(ah\nu)^2$  versus photon energy for direct transition.

**Fig.8** Current-voltage (J-V) characteristics of (a) pristine TNAs, (b)U-PbS/TNAs, (c)A-PbS/TNAs, (d)V-PbS /TNAs and (e) N- PbS/TNAs.

**Fig.9.** Photocurrent attenuation curves of (a) Pristine TNAs, (b) U-PbS/TNAs, (c) A-PbS/TNAs, (d) V-PbS/TNAs and (e) N-PbS/TNAs. The inset is photocurrent decay rate histograms.

**Fig.10.** Electrochemical impedance spectroscopy plots of (a) Pristine TNAs, (b) U-PbS/TNAs, (c) A-PbS/ TNAs, (d) V-PbS/TNAs and (e) N-PbS/TNAs. The inset is the enlarged range at high frequency region for the samples (a) and (b).

**Fig.11.** Mott-Schottky curves of the (a) Pristine TNAs, (b) U-PbS/TNAs, (c) A-PbS/ TNAs, (d) V-PbS/TNAs and (e) N-PbS/TNAs.

Figure 1

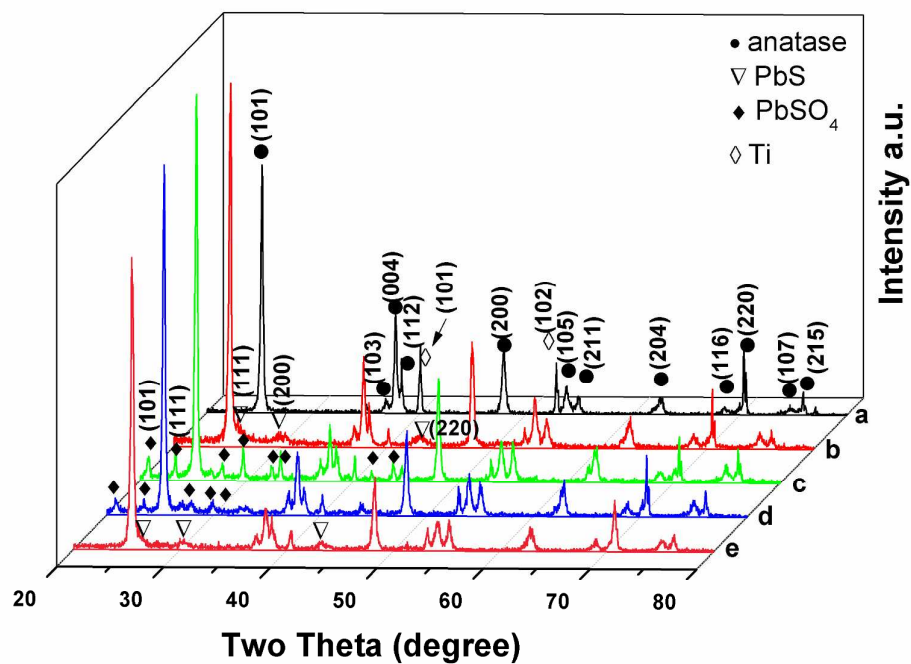


Figure 2

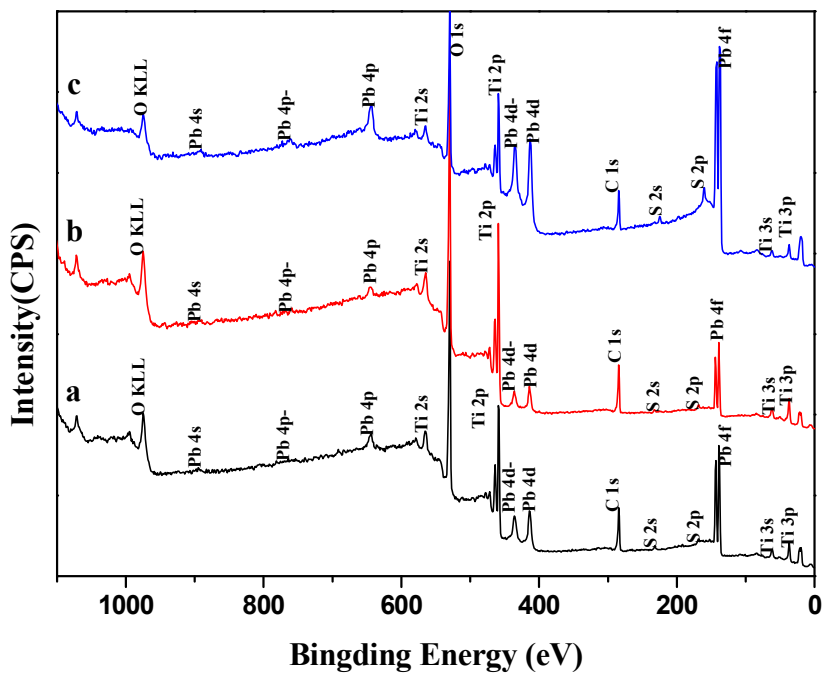


Figure 3

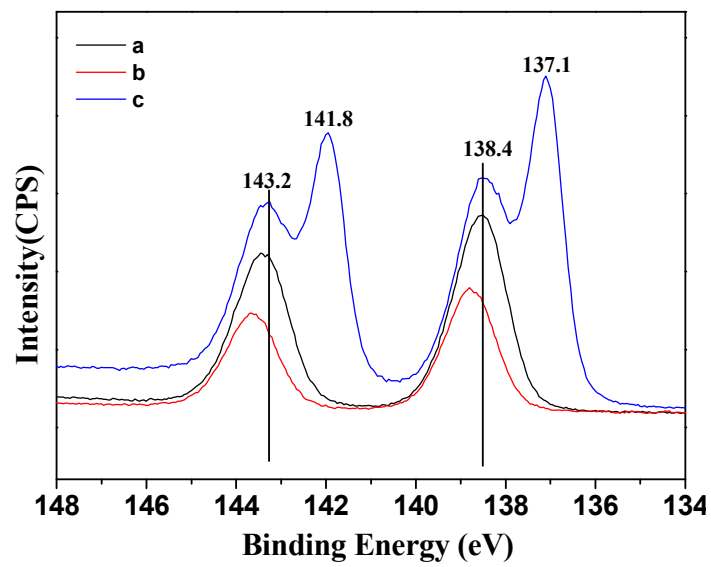


Figure 4

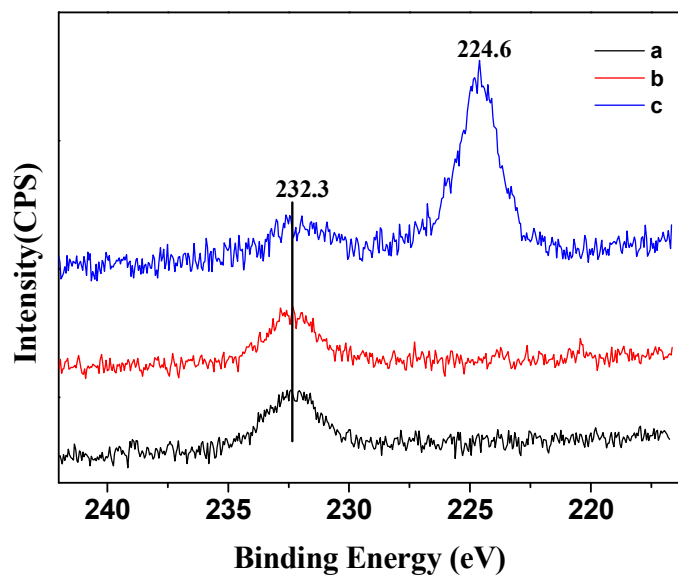


Figure 5

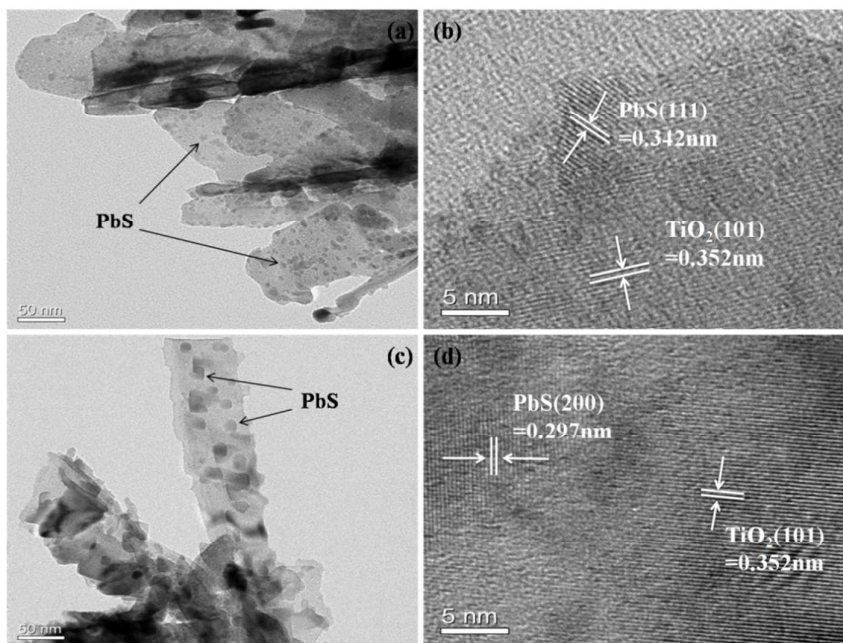


Figure 6

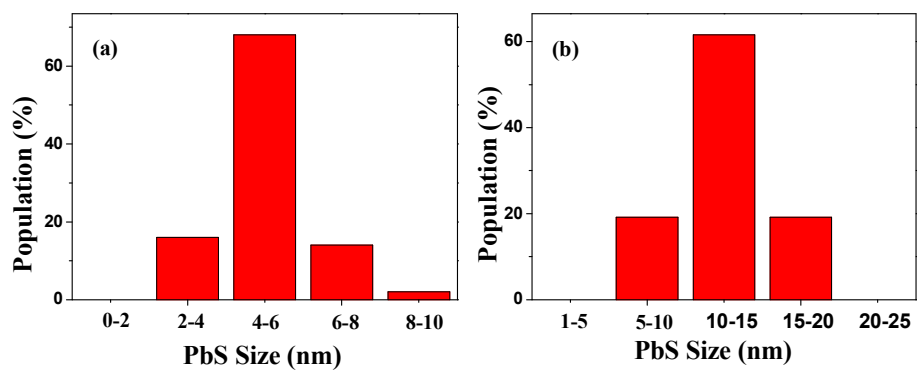


Figure 7

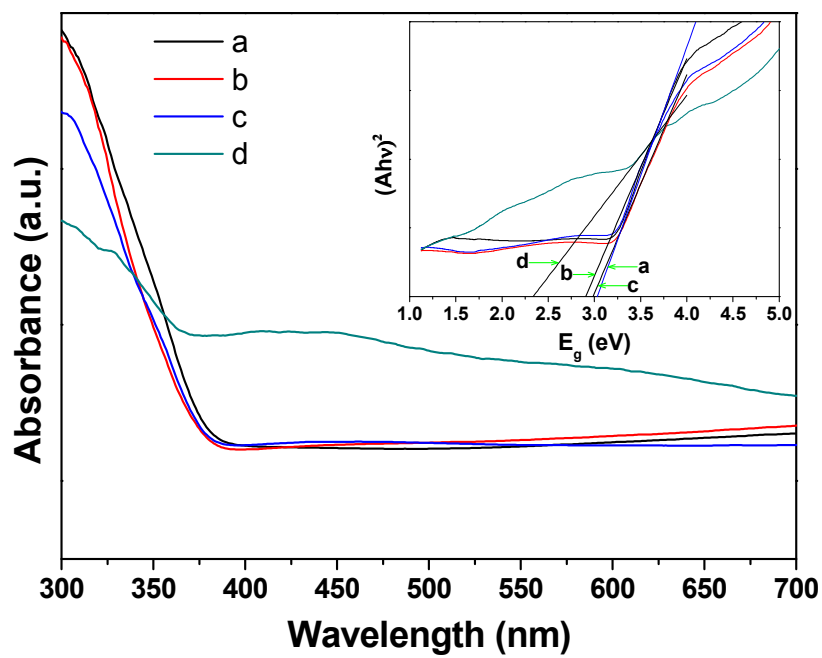


Figure 8

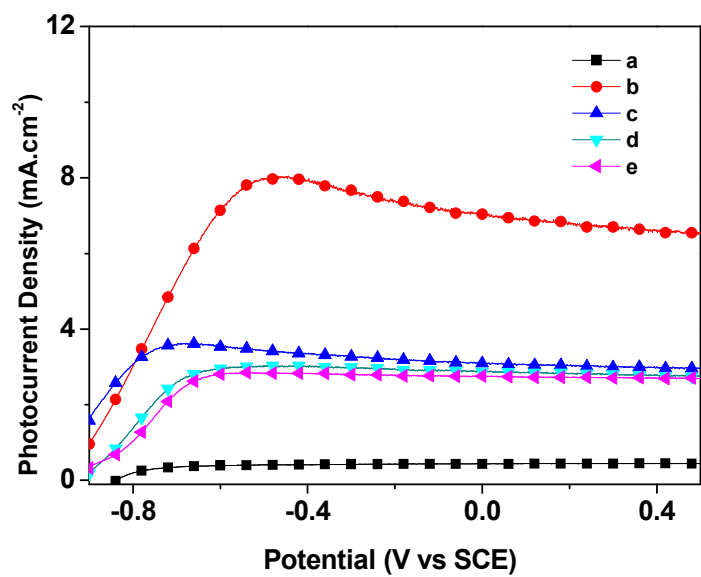


Figure 9

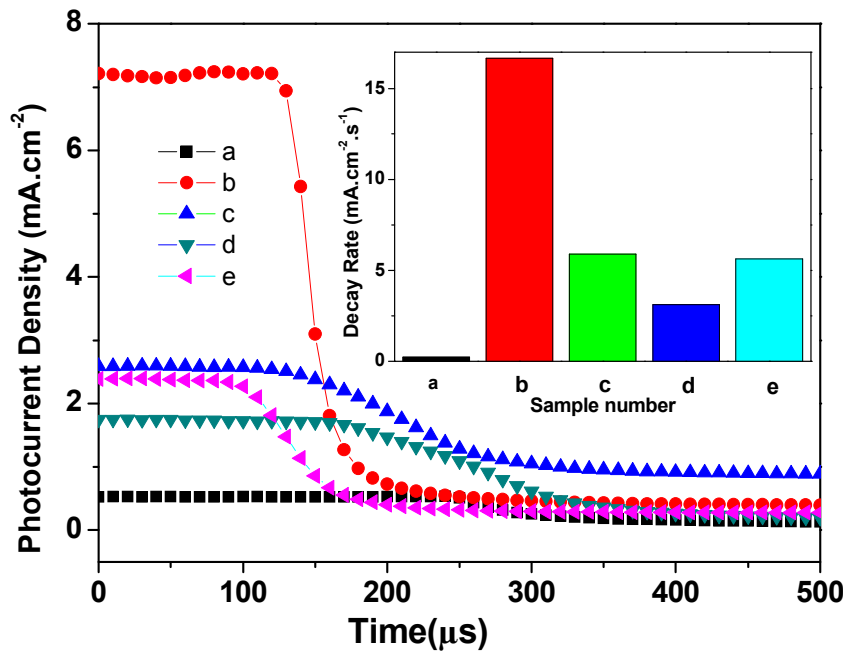


Figure 10

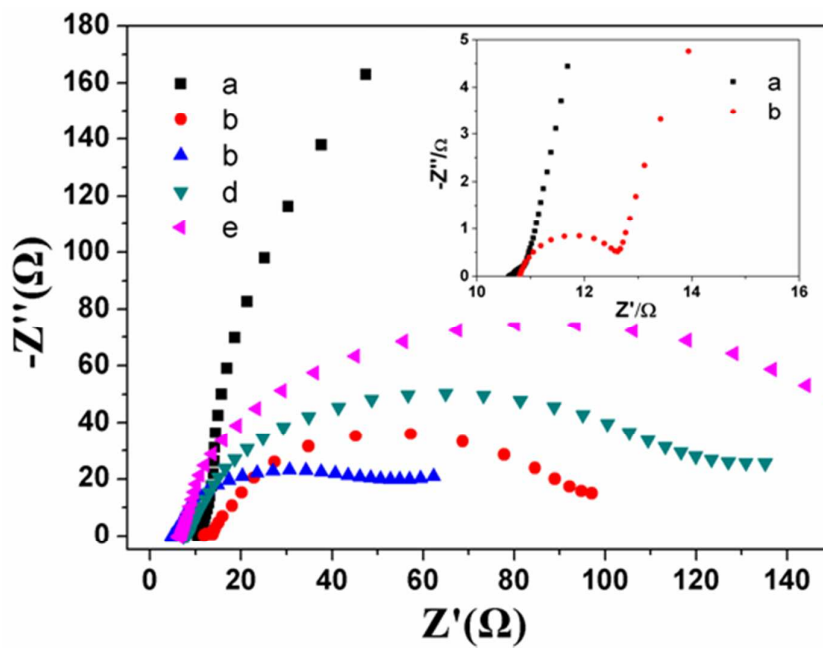
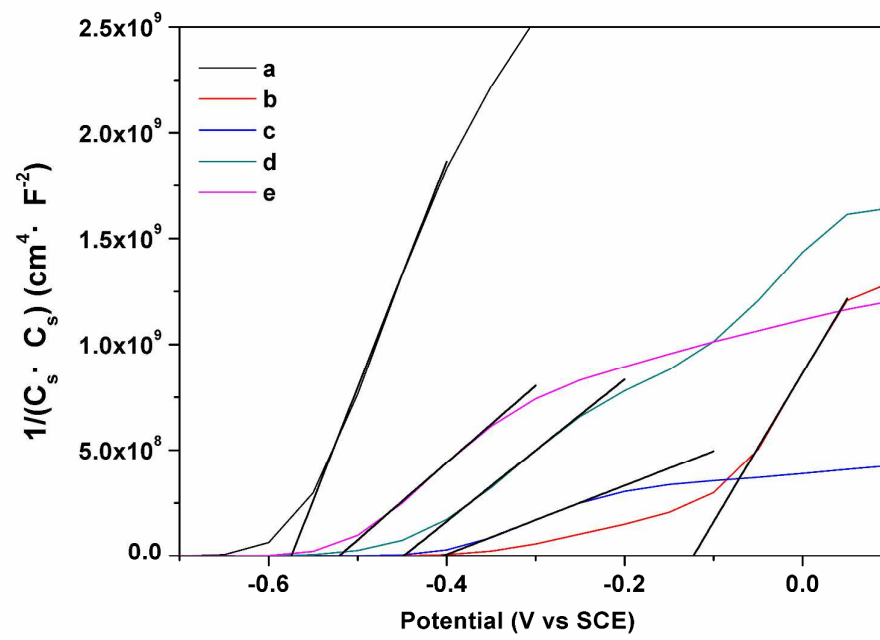


Figure 11



**Tab.1.** Simulated values of the devices in equivalent circuits of the samples

Sample	R ( $\Omega \cdot \text{cm}^2$ )	R <sub>1</sub> ( $\Omega \cdot \text{cm}^2$ )	C <sub>1</sub> (F.cm <sup>-2</sup> )	R <sub>2</sub> ( $\Omega \cdot \text{cm}^2$ )	C <sub>2</sub> (F.cm <sup>-2</sup> )	R <sub>3</sub> ( $\Omega \cdot \text{cm}^2$ )	C <sub>3</sub> (F.cm <sup>-2</sup> )	R <sub>w</sub> ( $\Omega \cdot \text{cm}^2 \cdot \text{s}^{-1/2}$ )
Prinetime TNAs	8.328	10.2	0.02309	-	-	730.9	0.007296	0.1289
N-PbS/TNAs	8.462	0.5479	0.0002987	165.8	0.009803	34.67	0.01654	0.1489
U-PbS/TNAs	16.64	85.33	0.01013	2.45	0.0000921	14.31	0.01533	0.1523